Ultrasound in Med. & Biol., Vol. ■, No. ■, pp. 1–12, 2017

0301-5629

http://dx.doi.org/10.1016/j.ultrasmedbio.2016.11.015

● *Original Contribution*

CARDIAC SHEAR WAVE VELOCITY DETECTION IN THE PORCINE HEART

Hendrik J. Vos,[*][†] Bas M. van Dalen,[‡] Ilkka Heinonen,[§][¶][||] Johan G. Bosch,[*] Oana Sorop,[§]
Dirk J. Duncker,[§] Antonius F. W. van der Steen,[*][†][#][**] and Nico de Jong[*][†][||]

[*] Biomedical Engineering, Erasmus MC, Rotterdam, The Netherlands; [†] Acoustical Wavefield Imaging, Delft University of Technology, Delft, The Netherlands; [‡] Cardiology, Erasmus MC, Rotterdam, The Netherlands; [§] Experimental Cardiology, Erasmus MC, Rotterdam, The Netherlands; [¶] University of Turku and Turku University Hospital, Turku, Finland; [||] Department of Clinical Physiology and Nuclear Medicine, University of Turku and Turku University Hospital, Turku, Finland; [#] Netherlands Heart Institute, Utrecht, The Netherlands; and [**] Shenzhen Institutes of Advanced Technology, Chinese Academy of Sciences, Shenzhen, China

(*Received* 16 *May* 2016; *revised* 8 *November* 2016; *in final form* 19 *November* 2016)

Abstract—Cardiac muscle stiffness can potentially be estimated non-invasively with shear wave elastography. Shear waves are present on the septal wall after mitral and aortic valve closure, thus providing an opportunity to assess stiffness in early systole and early diastole. We report on the shear wave recordings of 22 minipigs with high-frame-rate echocardiography. The waves were captured with 4000 frames/s using a programmable commercial ultrasound machine. The wave pattern was extracted from the data through a local tissue velocity estimator based on one-lag autocorrelation. The wave propagation velocity was determined with a normalized Radon transform, resulting in median wave propagation velocities of 2.2 m/s after mitral valve closure and 4.2 m/s after aortic valve closure. Overall the velocities ranged between 0.8 and 6.3 m/s in a 95% confidence interval. By dispersion analysis we found that the propagation velocity only mildly increased with shear wave frequency. (E-mail: h.vos@erasmusmc.nl)

Key Words: **Echocardiography, Stiffness measurements, Shear wave elastography, High-frame-rate imaging, Valve closure.**

INTRODUCTION

Heart failure is a major public health problem in developed countries. Chronic heart failure is a highly disabling and life-threatening condition: Patients experience dyspnea and fatigue, and 1-y mortality rates range from 10% to 20%. The prevalence increases rapidly with age, reaching over >10% for those aged >75 y (Mosterd et al. 1999). In patients with heart failure with preserved ejection fraction, left ventricular stiffening is presumed to be one of the important causes responsible for the symptoms and poor prognosis. Currently, there is no accurate non-invasive method for diagnosing left ventricular stiffening, as blood biomarkers are non-specific and current ultrasound imaging methods have low specificity and sensitivity (Paulus et al. 2007; van Dalen et al. 2016). Yet, early recognition of the decreasing condition of the heart, for example, in diabetic or hypertensive patients, could facilitate prompt initiation of personalized medicine (*e.g.,* angiotensin-converting enzyme [ACE] inhibitors, beta blockers, diuretics) and/or a change in lifestyle ("good food, good movement, good sleep and good attitudes") and thereby prevent or delay the progression toward overt heart failure.

The literature over the past 15 y reports the use of shear waves for tissue stiffness measurements, so-called shear wave elastography, based on either magnetic resonance or ultrasound imaging. It is targeted mainly at radiology applications such as liver cirrhosis and breast cancer diagnosis (Parker et al. 2011). The suspected correlation between diastolic dysfunction and myocardial stiffness led to several ultrasound studies on the use of shear waves to measure the myocardial stiffness (Bouchard et al. 2009; Hollender et al. 2012; Kanai 2005; Song et al. 2013; Urban et al. 2013; Vos et al.

Address correspondence to: Hendrik J. Vos, Biomedical Engineering Ee2302, Erasmus MC, PO Box 2040, 3000-CA Rotterdam, The Netherlands. E-mail: h.vos@erasmusmc.nl

2015), generally using minimally invasive approaches, such as intracardiac catheters, to highly invasive approaches, including measurements in open-chest animal models. The waves occur naturally after closing of the valves, which also leads to the regular heart tones (Brekke et al. 2014; Kanai 2009; Pernot et al. 2007). Moreover, the atrial-systolic wave (*i.e.,* atrial-kick wave), which occurs in late diastole, has been studied recently by Pislaru et al. (2014). They reported the propagation of a wave front along the anterior left ventricular wall with a propagation velocity that correlates well to the derived diastolic elasticity of the wall. Alternatively, the waves can be induced by external sources (Bouchard et al. 2009; Hollender et al. 2012; Song et al. 2013; Urban et al. 2013). Shear waves in soft biological tissue have a propagation velocity of 1–10 m/s, and this velocity is influenced by the stiffness of cardiac tissue (Couade et al. 2011; Kanai 2005; Urban et al. 2013).

During each heartbeat, shear waves are generated at two different time points: after mitral valve closure, and after aortic valve closure. The first occurs in early systole, the second in early diastole. This means that muscle stiffness can be measured in both the relaxed and contracted states, potentially providing relevance for both diastolic and systolic phases.

The limited length of the septal wall (~4 cm) and the propagation velocity of these waves imply that the events generally last 10–25 ms and 50 ms at most. Hence, to visualize the waves and accurately measure their propagation velocity by tracking the wave pattern on at least a few frames, the frame rate should reach >500 frames/s. Specialized ultrasound equipment is needed that can sustain a very high frame rate on the order of 1000–5000 frames/s, compared with the 20–100 frames/s of conventional ultrasound scanners. Such high-frame-rate detection techniques (Bercoff et al. 2011; Brekke et al. 2014; Hansen et al. 2014; Holfort et al. 2008; Kruizinga et al. 2012) are made possible by the more recent development of multichannel acquisition equipment, in which all data from the probe are digitized and made available for software-based image reconstruction.

To our knowledge, cardiac shear wave measurements immediately after closure of both the aortic and mitral valves have not been studied quasi-simultaneously and in a non-invasive manner, to date. In the work described here, we explored the naturally occurring shear waves in the porcine septal wall produced by aortic and mitral valve closure using high-frame-rate ultrasound recordings and subsequent shear wave imaging. Measurements were performed on a closed chest under light sedation. The primary aim was to estimate wave propagation velocity and frequency content, as a first step toward actual non-invasive stiffness measurements. In addition, we studied dispersive wave propagation effects of the shear wave and the implications of such dispersion on the accuracy of the methods used to extract the shear wave propagation velocity from the data.

METHODS

Concept

In a bulk elastic material the shear wave velocity C_s depends on the density of the material ρ and the shear modulus μ:

$$C_s = \sqrt{\mu/\rho} \tag{1}$$

Application of this equation to actual shear wave propagation in cardiac tissue is probably too simplistic. Cardiac fiber orientation varies across the septal wall, featuring two regions of different anisotropy (Jiang et al. 2007), which may result in anisotropic shear wave propagation as observed with radiation force-induced shear wave elastography (Couade et al. 2011). Furthermore, viscous loss will introduce dispersion (Bercoff et al. 2004b), and the finite wall thickness may lead to dispersive Lamb waves (Kanai 2005; Nenadic et al. 2011). Moreover, the shear modulus varies in time throughout the cardiac cycle (Couade et al. 2011), with presumably the strongest variation in early systolic and early diastolic phases, which mark the onset of contraction and relaxation. Nonetheless, the equation illustrates that shear modulus and shear wave propagation do have a monotonic relationship in which a higher propagation velocity is expected for a higher shear modulus (*i.e.,* stiffer material).

We extracted the shear waves on the septal wall after mitral valve and aortic valve closure. Shear waves have a particle displacement oriented perpendicularly to the direction of propagation. In soft biological tissue, the *propagation* velocity is on the order of 1–10 m/s. The *local particle* velocity of the shear waves is much lower, on the order of 0.1–3 cm/s. Tissue Doppler imaging is used to detect this local particle velocity. Because Doppler is most sensitive to axial motion, it can best detect shear waves propagating laterally in the field of view, at a tissue Doppler image (TDI) velocity scale adapted to match the local particle velocity. Translating these properties into clinical echocardiography, a TDI system would be most sensitive to shear waves traveling through the interventricular septal wall in a long-axis parasternal view, rather than in an apical view. Hence, we used the parasternal view to detect the waves after valve closure.

Animal model and preparations

The study was approved by the Erasmus MC Animal Experiments Committee (DEC 109-12-22), and all experiments were performed in accordance with the National Institutes of Health *Guide for the Care and Use of*

Laboratory Animals (National Research Council 2011). This study used 22 healthy Göttingen minipigs (28 ± 6 kg), at approximately 1 y of age. Pigs were sedated with an intramuscular injection of Zoletil (tiletamine/zolazepam, 5 mg/kg) and xylazine (2.25 mg/kg) approximately 10 min in advance of the high-frame-rate measurements. They were placed on their right side and were breathing naturally. The hair on the skin area around the sternum was shaven off to avoid reduction of acoustical transmission. Ultrasound gel was applied on the skin. The probe was inserted into a disposable ultrasound sleeve (intra-operative transducer cover, 15 × 244 cm, REF 1238-02, Probetection, Palmedic, Lichtenvoorde, Netherlands).

Data acquisition

The probe was positioned such that the mitral valve, aortic outflow tract and septal wall were visible in a transthoracic parasternal long-axis view (see Fig. 1). Raw channel data were captured with a research scanner (SonixTOUCH, Ultrasonix/Analogic Ultrasound, Richmond, BC, Canada), an SA4-2 phased array probe and data-acquisition module (SonixDAQ, Ultrasonix/Analogic Ultrasound) for full channel data capture. Simultaneously, data were acquired and processed with the internal SonixTOUCH ultrasound engine to produce on-screen B-mode images for direct feedback to the clinician. The transmission pulse was a 2.5-MHz, 1.5-cycle pulse at a repetition frequency of 4000 Hz (leading to 4000 frames/s). To create an optimal diverging wave that illuminates the entire field of view within one transmission, we chose a transmission from three central elements in the probe. The signal-to-noise ratio in the tissue echo was sufficient for tissue motion tracking.

The SonixDAQ recorded the channel data from the probe at a sampling rate of 40 MHz, 6236 samples per trace, analogue-to-digital conversion sampling depth of 12 bits, 21-dB gain in the internal low-noise amplifier and 27-dB gain in the programmable gain amplifier. This combination of gain and sampling depth was sufficient to avoid signal clipping during analogue-to-digital conversion in the limited depth range where the septal wall was located (2–6 cm). The sampling clock of the DAQ was synchronized to the internal clock of the ultrasound engine, which produced the frame trigger and the transmission pulse. The data (8 GB per recording, 10,758 frames) were stored to disk for off-line processing. The recording time was 2.7 s, which corresponded to two to four full heartbeats at a general heart rate between 70 and 90 bpm.

Tissue velocity extraction

A full frame was reconstructed from each transmit through a custom imaging algorithm in the frequency–wavenumber domain for plane waves (Kruizinga et al. 2012; Lu 1997; Volker 2014). The implementation automatically returns the analytical signal $S(x, z, i)$ in frame i for every pixel at (x, z) through the Hilbert transform in the axial direction. In what follows, the (x, z) coordinates within the brackets are omitted for simplicity of the equations. Local tissue velocity $v(i)$ was obtained with one-lag autocorrelation for every pixel (based on Brekke et al. 2014),

$$R_1(i) = S(i) \cdot S^*(i-1) \tag{2}$$

$$v(i) = \frac{\angle R_1(i)}{\pi} v_{\mathrm{N}} \tag{3}$$

$$v_{\mathrm{N}} = \frac{\lambda}{4} F \tag{4}$$

in which R_1 is the one-lag autocorrelation value for a time offset of 1 frame, an * denotes the complex conjugate, $\angle$ denotes the angle {rad}, v_{N} is the Nyquist velocity and wavelength $\lambda = c/f_{\mathrm{c}}$, where f_{c} is the center frequency of the pulse, c is the (longitudinal) speed of sound in the medium, and F is the frame rate. The value of the Nyquist

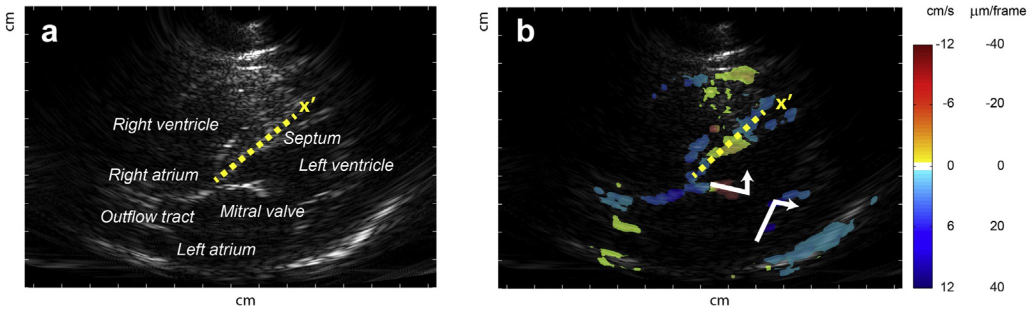

Fig. 1. (a) Example of a gray-scale image of a pig heart in diastole, with anatomic annotations. The anatomic M-mode line in the septal wall is represented by the *yellow line*. (b) Tissue velocity image obtained with the one-lag autocorrelation technique. *White arrows* denote the motion of the valve leaflets upon the onset of the atrial contraction.

velocity was 0.61 m/s, which avoided any aliasing effect in the cardiac tissue velocity measurements.

As done by Brekke et al. (2014), we applied a spatial smoothing filter to the autocorrelation frames calculated with eqn (2). This smoothing consisted of convolution of the frames with a boxcar window kernel with a size of 2.5 mm in both axial and lateral directions. Because the speckle size in the axial direction was on the order of 1.3 mm, such a moving average filter reduced the effects of speckle and noise on the velocity estimates. Because the wavelength of the mechanical waves was at least 10 mm, the chosen kernel size did not reduce the signal levels significantly.

For each heartbeat in the full recording, the moment of mitral valve closure and moment of aortic valve closure were detected manually. This moment was taken either as the moment when the valve leaflets visibly touched each other on closure and/or when the color of the leaflets in the tissue color Doppler movie changed rapidly, revealing sudden deceleration of the leaflets. Where the aortic valve was not visible, the moment when the first sign of a wave was present on the basal part of the septal wall was selected. Three hundred frames were isolated around these events, covering a period of 75 ms. During this period no gross motion of the heart was visible because a valve closure marks the onset of an isovolumetric phase in the cardiac cycle, in which cardiac motion is minimal. In the tissue velocity frames, an anatomic M-mode line was manually placed at the endocardial border of the septal wall (Fig. 1). The length of the M-mode line was set to cover the full visible propagation of waves in the septal wall. This resulted in a length of about 2.5 cm in early diastole and about 3.5 cm in early systole, dictated by the contracted and elongated states of the septal wall, respectively. The basal part of the septal wall typically moved about 1 cm in both lateral and axial directions between the two events.

Shear wave analysis

To accurately visualize and track the shear waves along the septal wall, we gathered the tissue motion in a 2-D panel, as reported earlier (*e.g.,* Bercoff et al. 2004a; Brekke et al. 2014; Hollender et al. 2012). With reference to Figures 1 and 2, the tissue velocity along the M-mode line in each of the 300 frames was extracted and stacked vertically to compose a 2-D panel. This panel displays the tissue velocity in space and time, and shear waves appear as tilted wave patterns in this panel. The slope ($\Delta x'/\Delta t$) of the wave pattern corresponds to the shear wave propagation velocity. The slope was analyzed with a Radon transform (Urban and Greenleaf 2012; Vos et al. 2015), calculated at angular steps of 0.25°. Normalization in the Radon domain was achieved by division of the data in the Radon domain by the Radon transform of an image of equal size and containing unit values only. This normalization avoided an apparent bias in the analysis caused by the square image domain instead of a presumed circular domain in the Radon implementation used (MATLAB R2012b, The MathWorks, Natick, MA, USA). The peaks in the Radon domain were detected with a regular global peak searching algorithm. Taking the peak maximum value for the early-systolic wave and the peak minimum value for the early-diastolic wave produced the most reliable results, based on visual verification of the results. The angular location of the peak indicated the slope of the main axis of propagation of the wave pattern. The data were pre-processed with a linear detrending operation, followed by a zero-phase fourth-order Butterworth band-pass filter with −6-dB cutoff points at 15 and 150 Hz and mild tapering in the temporal direction. Values outside of the velocity range (0 m/s, 10 m/s) were considered non-physical values caused by analysis errors and, therefore, were removed from the results before averaging the recorded velocities per animal. This removed 20% of the

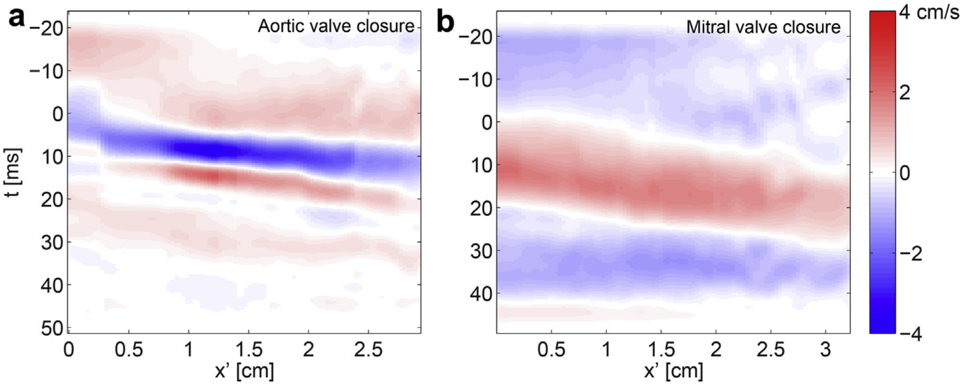

Fig. 2. Tissue velocity panels obtained at the M-mode line in the septal wall after (a) aortic valve closure, that is, early diastole, and (b) mitral valve closure, that is, early systole.

single-heartbeat events after mitral valve closure and 12% after aortic valve closure.

In search for the highest precision in the Radon method, we applied the method to both the tissue velocity data and the tissue acceleration data, obtained by the time derivative of the tissue velocity. We expected that slow global motion of the cardiac wall was suppressed in the tissue acceleration data while maintaining the faster shear wave motion. However, we observed that the standard deviation of shear wave detections after mitral valve closure increased by a factor of 1.5, likely caused by the lower wave amplitudes and lower frequency content of these waves. On the other hand, the standard deviation of shear wave detection after aortic valve closure decreased by a factor of 1.5. Yet, to maintain equal analysis for both mitral valve and the aortic valve closure, we selected the tissue velocity data to obtain the shear waves in all cases.

Spectral analysis

The spectral density of the shear waves for each valve-closing event was calculated by taking the mean of the absolute value of the spectral content for each pixel along the anatomic M-mode line. Wave velocity dispersion was investigated through a Radon transform after temporal bandpass filtering of the tissue velocity panels. The bandpass filters were fourth-order zero-phase Butterworth filters with the following bandpass frequencies: 15–45, 45–75, 75–110 and 110–150 Hz. The results are illustrated in a box-and-whisker plot.

RESULTS

Imaging

Figure 1a provides an example of a gray-scale image of the heart obtained in the parasternal long-axis view with anatomic annotations. The septal wall is located at a depth of 5 cm, and its endocardial side is marked with a *yellow line*. This line is the anatomic M-mode line at which the tissue velocity is extracted. The apex is not visible in such a parasternal view. The delineation of the structures in the heart is relatively poor compared with conventional sector scan images; this is caused by the single diverging wave transmission in our method. Yet, as seen in Figure 1b, the processing of the radiofrequency (RF) frames to reveal the local instantaneous tissue velocity through eqns (2)–(4) reveals consistent areas of up-moving tissue (*red coloring*), down-moving tissue (*blue coloring*) and low motion (*green coloring*). The example is taken when the mitral valve is opening (as annotated by the *arrows* in Fig. 1b), leading to *red coloring* of the top leaflet and *blue coloring* of the bottom leaflet. At that instant, the basal part of the septal wall moves away from the probe, leading to the *blue coloring*. For the purpose of clarity in this image, a mask was applied to the tissue velocity based on the magnitude of both the gray-scale value and the tissue velocity value (6 mm/s).

Shear wave analysis

We observed mechanical shear waves after valve closure in all 22 recordings. Figure 2a is an example of the wave pattern after aortic valve closure. The pattern is clearly visible, lasting one and one-half cycle and having a magnitude of tissue velocity of about 2 cm/s. At a relative time of $t = 12$ ms, half a wave fits in about 2 cm, indicating a wavelength of about 4 cm. A full cycle lasts about 10 ms (100 Hz). Such values correspond to a propagation velocity of 4 m/s, which is consistent with the inversed slope of the arrow (approximately 2.5 ms/cm in Fig. 2a). The peak tissue displacement between two frames was 5 μm (at $t = 10$ ms in Fig 2a), directed downward. By integrating the displacement over time (not shown), we could estimate the overall peak tissue displacement. This resulted in a peak tissue displacement of about 100 μm, occurring at $t \sim 10$ ms.

The wave occurring after mitral valve closure (Fig. 2b) was less clear in the velocity panel because of the smaller amplitude (on the order of 1.5 cm/s) and lower temporal frequency in the spatial domain of 3.3 cm. The peak tissue displacement between two frames was 3 μm (at $t = 15$ ms in Fig. 2b), directed upward. The overall peak tissue displacement was about 200 μm, occurring at $t \sim 25$ ms. The wavelength was estimated to be 8 cm (slightly less than half a wave fitting in the spatial domain of 3.3 cm), and a full cycle lasts about 40 ms (25 Hz). Combining such values leads to a propagation velocity of about 2 m/s of the wave.

When the time derivative of the data is taken, which leads to the tissue acceleration panels in Figure 3, the wave after aortic valve closure is clearly visible. The peak acceleration is on the order of 10 m/s^2. As the time derivative operation leads to a gain that increases linearly with frequency, the low-frequency wave after mitral valve closure is hardly visible in the tissue acceleration panel, and high-frequency noise becomes clearly visible. These results suggest that acceleration panels may be useful for tracking the waves after aortic valve closure, but not after mitral valve closure. For consistency, we chose to use the tissue velocity data for the shear wave analysis for both types of events.

Figure 4 provides examples of tracking of the waves with the Radon transform. Because of the opposite directions of the dominant tissue motion during the wave, that is, upward for mitral valve closure and downward for aortic valve closure (*cf.* Fig. 4a,b), we tracked the up-going half-cycle and down-going half-cycle, respectively. According to the principles of tracking a wave through

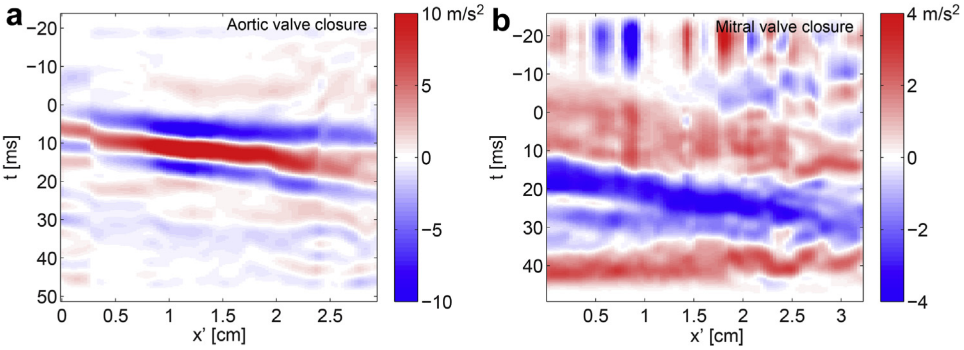

Fig. 3. Tissue acceleration panels obtained at the M-mode line in the septal wall after (a) aortic valve closure, that is, early diastole, and (b) mitral valve closure, that is, early systole.

the Radon transform, the line represents the most likely linear path of the velocity peak.

The results of the wave propagation velocities obtained with the Radon transform and particle velocity analysis are illustrated in Figure 5. The measured values over subsequent heartbeats were averaged to obtain a single value per examination. The 22 recordings resulted in 18 reliable (defined by 0 m/s $< C_s <$ 10 m/s) estimates after mitral valve closure and 21 after aortic valve closure. The waves after mitral valve closure had a median velocity of 2.2 m/s (90% interval: 0.8–3.2 m/s), whereas the waves after aortic valve closure had a median velocity of 4.2 m/s (90% interval: 1.4–6.3 m/s).

Although no proof has yet been provided in the literature, both the difference and ratio of the wave velocities after aortic and mitral valve closure may be of clinical relevance. Figure 6 illustrates both the paired difference and paired ratio between aortic valve closure and mitral valve closure velocities. The difference has a mean value of 2.1 m/s with a standard deviation of 1.4 m/s, which is significantly different from zero ($N = 18$, $p < 0.001$, two-sided *t*-test). Its median value is 1.8 m/s. The paired ratio was 2.1 on average, with a median value of 1.9. Such increased wave propagation velocity after aortic valve closure would imply greater stiffness in that part of the cardiac cycle.

Spectral analysis

The spectral density graphs (Fig. 7) illustrate various trends. The velocity energy density is flat up to 25 Hz and then decreases monotonically with increasing frequency in the tissue velocity panels (Fig. 7a,b). The median value ranges from 0.3 to 7, which is a factor of about 20. Ninety percent of the values are in a band that is limited by a factor of 0.5 below, and 2 above, the median. This range indicates that the wave amplitude is always on the order of the tissue velocities exemplified in Figure 4, that is, one or a few centimeters per second.

When taking the time derivative, that is, analyzing particle acceleration data, differences between aortic valve closure and mitral valve closure appear more clearly. A peak in the frequency content after mitral valve closure appears at around 40 Hz, and after aortic valve closure, at around 80 Hz. Such values are well within the frequency range of audible heart tones (Arnott et al.

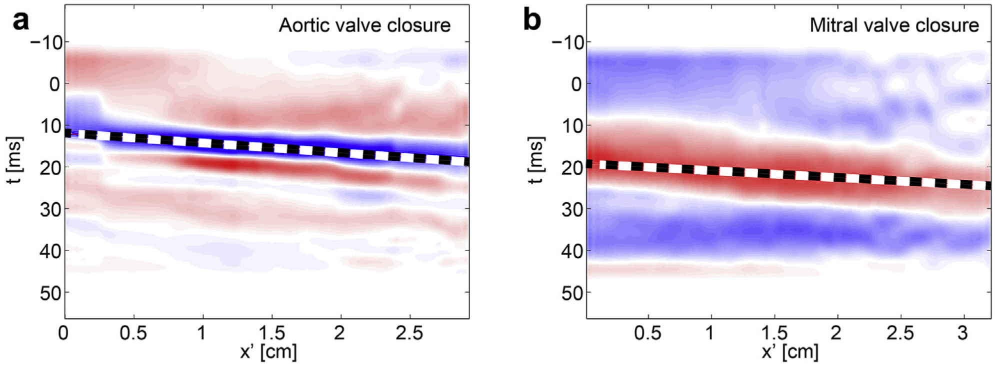

Fig. 4. Tissue velocity panels (same data as in Fig. 2) in which the result of the wave tracking with the Radon transform is depicted by the dashed line. (a) After aortic valve closure, that is, early diastole, and (b) after mitral valve closure, that is, early systole.

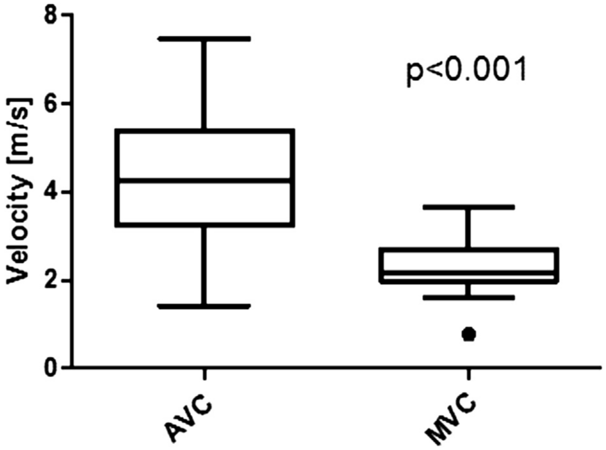

Fig. 5. Shear wave velocity measurements obtained with the Radon transform for all pigs. In this and the remaining figures, the whiskers are plot according to Tukey's method. AVC = aortic valve closure, MVC = mitral valve closure.

1984). The different locations of the peaks are consistent with the different appearance of the wavelets in the data in Figures 2 and 3.

In Figure 8 are examples of the normalized tissue velocity panels after bandpass filtering. The relatively narrow bandpass filters lead to larger ringing of the data, which does not pose any problems for the Radon velocity estimator applied to these data. The high-frequency filtered waves after mitral valve closure (Fig. 8b) exhibit greater interference with other low-amplitude signals, which hampers accurate tracking of the wave pattern.

Figure 9 illustrates the grouped results of tracking the wave pattern for all available data, after bandpass filtering in the four frequency bands. Despite the relatively large spread in the data, we can extract general trends that are relevant to shear wave analysis methods. The phase velocity is about 4 m/s after aortic valve closure, with only a mild increase with shear wave frequency. The phase velocity is about 2 m/s after mitral valve closure and increases to slightly higher values for frequencies >60 Hz. However, the interquartile range also rapidly increases for frequencies >60 Hz, indicating the large spread in the data. For these frequencies, the amplitude of the signal has become small (*cf.* Fig. 7), leading to an increased chance of tracking noise rather than the wave itself (*cf.* Fig. 8b). The general observations, despite the variance, are that (i) the phase velocity does not go to zero velocity for decreasing frequency, and (ii) the dispersion is only mild. The implications are discussed below.

DISCUSSION

Methods

The systematic study of shear waves in the septal wall of 22 resting porcine hearts revealed median propagation velocities of 2.2 m/s after mitral valve closure and 4.2 m/s after aortic valve closure. These values are close to those reported earlier with acoustic radiation force (ARF)-based intracardiac shear wave measurements in large-animal models: Hollender et al. (2012) reported 1.4 and 4.1 m/s, respectively, and Couade et al. (2011) reported 1.45 and 4.8 m/s. The values are also close to shear wave propagation velocities, 1.5 and 4 m/s respectively, measured by continuous external wave excitation in the frequency range 50 to 100 Hz (Urban et al. 2013). In this context, we refer to our study as "passive" shear wave elastography (SWE) because we observe only the physiologic shear waves, compared with actively induced shear wave elastography based on ARF or continuous wave excitation. A difference between the two methods is the moment at which the shear wave velocity is measured. In our work, the early-systolic shear wave velocity (after mitral valve closure) is measured when the heart starts to contract, as the contraction is the cause of the closing of the mitral valve. Likewise, the early-diastolic shear wave

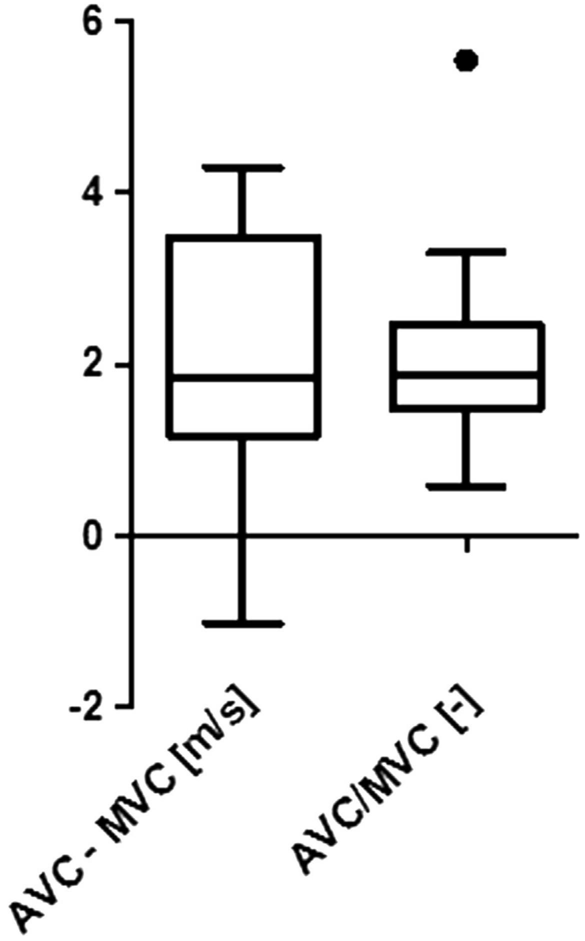

Fig. 6. Distribution of the difference between (AVC–MVC [M/s]) and ratio of (AVC/MVC) velocities after aortic valve closure (AVC) and mitral valve closure (MVC).

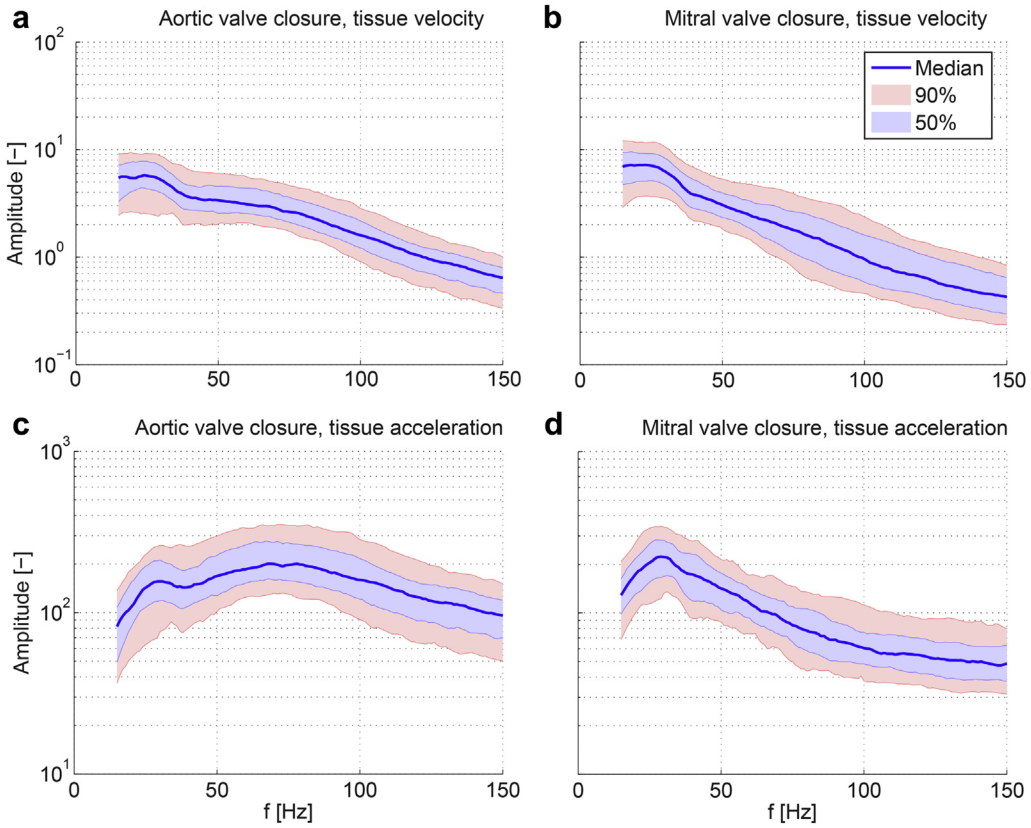

Fig. 7. Spectral content of the waves after (a, c) aortic valve closure and (b, d) mitral valve closure. Both (a, b) tissue velocity data and (c, d) tissue acceleration data are provided. The spectra were obtained from the raw data, that is, without frequency filtering.

velocity (after aortic valve closure) is measured when the heart has started to relax, as relaxation is the cause of the closure of the aortic valve. In actively induced SWE, the shear wave velocity is measured during the proper diastolic and systolic phases, in which the heart is fully relaxed and fully contracted, respectively. Nonetheless,

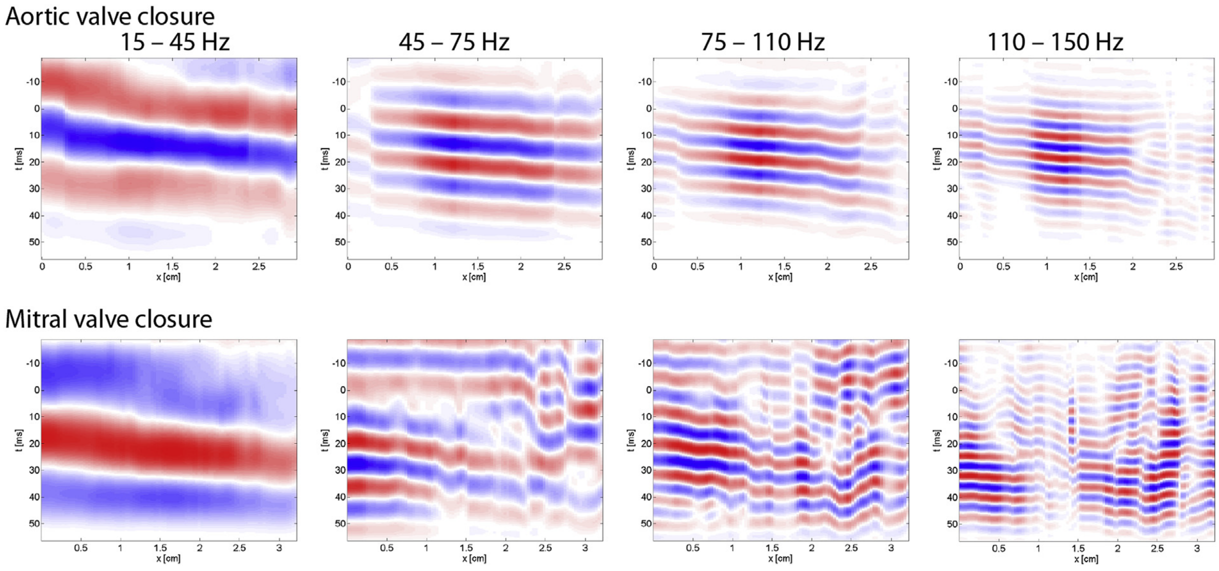

Fig. 8. Tissue velocity panels after filtering with bandpass filters with −6-dB cutoffs at 15–45, 45–75, 75–110 and

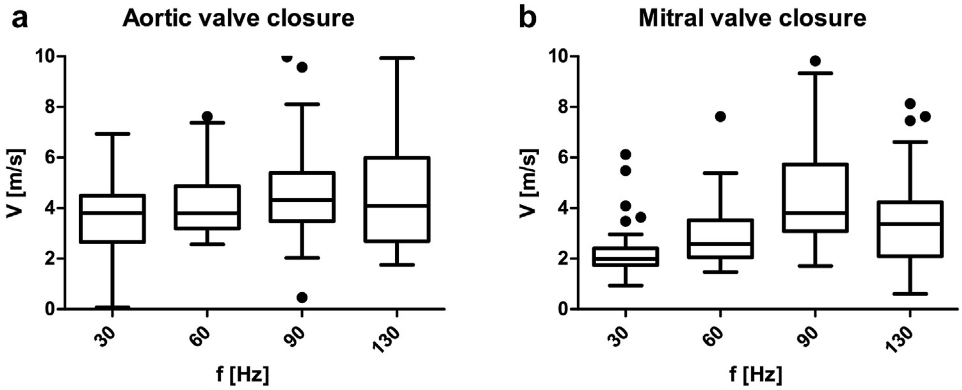

Fig. 9. Boxplots illustrating wave velocity dispersion after (a) aortic valve closure and (b) mitral valve closure, in the frequency ranges defined in Figure 8.

the strong similarity of the values suggests that the exact timing of the measurement is not critical in measuring early-diastolic and early-systolic myocardial stiffness.

It could be a point of discussion whether the observed wave phenomena are indeed the pure mechanical response to valve closure and not other possible phenomena like electromechanical waves induced by propagation of myocardial electrical conduction or gross cardiac motion is a topic for discussion. Several arguments support the hypothesis that the studied waves originate from valve closure. First, the valve closure could be accurately distinguished in the B-mode videos and in the accompanying color Doppler video (Supplementary Video 1, online only, available at http://dx.doi.org/10.1016/j.ultrasmedbio.2016.11.015); in all recordings we could see the mitral valve closure, and in about 50%, we could also see the aortic valve closure. The waves appeared within the first milliseconds (<5 ms) after visual confirmation of valve closure and originate from the location of the annular ring and aortic root. Second, there are reports that EM activation starts midway along the septal wall and then travels toward both the apex and base (Provost et al. 2011), which is opposite to the propagation direction of the observed waves in the basal part of the septal wall. Such a very high correlation of both time and space, and the consistent direction of wave propagation away from the valves, makes us confident that the valve closure is the source of the wave.

For the method to produce robust clinical values, determination of the propagation velocity needs to be precise. For this reason we studied several methods to track the wave pattern in the tissue velocity panels. The first was an analysis in the 2-D Fourier domain, which is especially useful in analyzing dispersion (Nenadic et al. 2013). Yet, the small spatial domain compared with the wavelength precluded the accurate use of a Fourier transform in the axial direction, as the effective resolution in *k*-space is determined by the actual spatial length. Two methods that did not require a spatial Fourier transform were a cross-correlation method and the Radon transform. In the temporal cross-correlation method (Vos et al. 2015), the shift in wave pattern over space and time leads to a shift of the peak in the correlation function. The cross-correlation technique operates on a time interval including any mechanical noise surrounding the main wave and, therefore, is sensitive to this noise. For each position, the shift of the peak was determined with a peak-searching algorithm, which resulted in an estimate of the average propagation velocity of the shear wave over space. The Radon transform tracks the rim of the wave, independent of any noise outside this rim (as visible in Fig. 4). By an initial analysis of the standard deviation obtained with these two methods, the lowest standard deviation was found with the Radon transform, which was especially true for the wave after mitral valve closure. The wave after aortic valve closure was consistently tracked with either method. Therefore, we used the Radon transform to analyze the data. By analyzing the standard deviation of propagation velocity within a single recording of two to four heartbeats, we estimated the relative standard deviation of a *single* measurement (*i.e.,* a single heartbeat) in the range 16% to 21% for both mitral valve closure and aortic valve closure. Such a standard deviation is similar to that reported in the literature within a group of six pigs using active shear wave elastography (Hollender et al. 2012). When our results are compared with literature values, a clear distinction should be made between shear waves that are induced externally and those that occur naturally after closing of the valves. With shear waves induced with an ultrasonic push (Bercoff et al. 2004a) or external vibration (Pislaru et al. 2009), the temporal frequency content of the waves is on the order of 100–500 Hz. With a given shear wave velocity on the order of 1–10 m/s, this leads to wavelengths that are 2–100 mm. Tracking such waves over a distance of few centimeters results in a relatively stable outcome, which therefore may provide a better basis for dispersion analysis in the 2-D Fourier domain. On the other hand, attenuation of shear waves at those frequencies is relatively high, challenging the analysis methods to take wave attenuation into account for accurate analysis.

As illustrated in Figure 9, the waves have a mildly dispersive nature: waves with lower temporal frequency have a lower propagation velocity than those with higher temporal frequency. A dispersive nature can be expected for waves with a few centimeters long on the septal wall with a thickness on the order of 0.5–1 cm; Such waves may be interpreted as guided Lamb waves (Nenadic et al. 2011), which regularly have frequency-dependent propagation velocities (*i.e.,* dispersive nature), contrary to bulk waves. A dispersive nature of waves can complicate the interpretation of shear wave elastography, because the simple relation given in eqn (1) does not hold anymore, and the temporal frequency content of the wave needs to be taken into account. In this respect, two directions can be followed to accurately relate any observed shear wave velocity to tissue stiffness. The first direction would be to isolate the wave in a relatively small frequency band and report the shear wave velocity in this frequency band. In this case, the shear wave velocity is an indirect measure of tissue stiffness. The second direction would be to interpret the dispersion with a parametric model of the wave. In following this direction, we compared the velocity dispersion in Figure 9 with a theoretical curve of asymmetric Lamb waves (Kanai 2005; Nenadic et al. 2011) and found that there is a very poor match: at lower frequency contents ($<$60 Hz), propagation velocity seems to be relatively high. The propagation velocity of asymmetric Lamb waves approaches zero for frequencies decreasing to zero, which does not correspond to the trend observed in our data (*cf.* Fig. 9). Therefore our data do not seem to be consistent with asymmetric Lamb waves, contradicting a relatively good fit reported earlier by Kanai (2005) in humans after aortic valve closure, in apical view. On the other hand, as discussed by Nenadic et al. (2011), mild dispersive behavior could correspond to viscous Rayleigh waves as well, which occur on the surface of two hemispheres one of which supports shear waves, and the other does not. Yet, such geometry is inconsistent with the geometry of the septal wall. Other effects like muscular anisotropy and non-smooth blood–tissue interfaces may violate the assumptions underlying Lamb wave physics, which assume a smooth wall and isotropic wave propagation. We recommend further study of the exact tissue motion during the wave propagation to reveal the dominant nature of the waves.

The dispersive relation has another implication for the tracking of the shear waves. As illustrated in Figure 3, the particle *acceleration* data after aortic valve closure reveal a clean wave, because low-frequency tissue velocity (such as that caused by the start of contraction/relaxation) is suppressed. However, the acceleration data after mitral valve closure are not improved, because of the lower-frequency contents of this wave. The resulting standard deviation was lower for the particle acceleration data after aortic valve closure, but higher for the acceleration data after mitral valve closure. Although it may be tempting to use the two different methods on the two separate effects, such an analysis may give a bias because the waves exhibit dispersion: taking a time derivative enhances the high-frequency components in the wave, leading to larger apparent wave velocities as tracked with the Radon transform. To avoid any such bias between aortic valve closure and mitral valve closure measurements, we chose to use the tissue velocity data throughout our analysis.

Our recordings also generally reveal a propagating wavefront on the septal wall after onset of the atrial-systole (“atrial kick”), in accordance with the observations by Pislaru et al. (2014). A preliminary analysis indicated that the propagation velocities are in the same range as those after mitral valve closure, which would be consistent with the hypothesis that the atrial kick produces a *mechanical* wave on the septal wall and consistent with the range of propagation velocities reported by Pislaru et al. However, because the atrial kick is not associated with the closure of valves or with any other abrupt phenomenon, the exact wave excitation mechanism is not clear to us. Moreover, based on our observation, we cannot exclude the possibility that the wave is caused by the electromechanical relaxation wave or any other phenomenon. Further study on abnormal hearts (such as those with atrial fibrillation) may be able to distinguish between a pure mechanical and electromechanical cause.

A possible cause of measurement inaccuracy is found in any misalignment between the image plane and the source of the waves. If the source of a diverging wave is not in the image plane, the apparent propagation velocity is larger. This can be mathematically represented as follows: If θ is the angle between the location of the source and the image plane, then the apparent propagation velocity is a factor $1/\cos(\theta)$ larger in the image plane. Hence, this effect will always lead to overestimation of the propagation velocity, not underestimation. The image plane in the current measurements was chosen to always have the mitral valve and aortic valve in its image. Yet, because of natural breathing, we cannot exclude that in some heartbeats (but not all beats in a single recording), the valves were not exactly in the image plane, which may have skewed the distribution in Figure 5 toward larger shear wave velocities.

In an earlier proceedings paper (Vos et al. 2015), we reported median velocities of 3.1 m/s after aortic valve closure and 1.9 m/s after mitral valve closure. The difference with the currently reported values is caused by an update in the data processing. We found that the Radon transform produced a significant bias in the estimated velocities when applied to an image with unequal numbers of pixels in its two dimensions. In the present study, this bias was avoided by two steps. First, the tissue velocity panel was resampled to have equal numbers of pixels in space and time. Second, we normalized the data in the Radon domain (see Shear Wave Analysis under Methods). We tested these steps on artificial tissue velocity panels with known propagation velocity and found that they indeed suppressed any bias in the Radon method of tracking the shear waves.

We used a single diverging wave transmission from few elements of the probe, which produces a relatively low resolution and low single-shot signal-to-noise ratio (SNR) compared with compounding techniques with larger-aperture diverging waves (Papadacci et al. 2014). However, because of the high frame rate of 4000 frames/s, we could apply temporal low-pass filtering in slow time to improve the SNR in the TDI frames. An alternative approach would be to use spatial compounding techniques (Papadacci et al. 2014), which would lead to higher SNR and resolution, with a reduced final frame rate.

Clinical implications

The results of this study support earlier claims that passive cardiac shear wave imaging is feasible *in vivo*. Yet, to establish clinical relevance, it is mandatory that the accuracy and precision of the outcome are sufficiently high. Our data indicate that single shear wave velocity measurements have a standard deviation on the order of 20%, consistent with other *in vivo* cardiac studies (Hollender et al. 2012; Urban et al. 2013). Such a standard deviation of a single measurement is likely too large to allow clinical decision making. However, the precision of the measurement can be increased by averaging, that is, by reducing the standard error of the mean. In that respect, the measurement can be repeated over several heartbeats, as was done in the current measurements. A recording time on the order of 10 s (*i.e.,* on the order of 10 heartbeats) is feasible to sustain with current tissue Doppler imaging techniques as implemented in high-end systems. This should reduce the standard error of the mean by a factor of 3 approximately, leading to better precision below 10%. Such a value is consistent with current accuracies of, for example, strain and tissue velocity measurements (Kjaergaard et al. 2006), and may be acceptable in actual clinical use.

Several clinical benefits characterize the method described here. First, the passive shear waves are present in the midcardiac wall, which is easy to image with regular transthoracic ultrasound. This implies good image quality even in obese patients. The relatively high SNR in the tissue Doppler panels, obtained with a single diverging wave generated with only a few elements in the probe, further indicates this benefit. Second, the method depends on valve closure, which occurs in most patients, including those with atrial fibrillation (AF). In current clinical decision trees used to diagnose heart failure, AF is a complicating factor in establishing flow ratios needed for the diagnosis of heart failure. AF occurs in 30% of all heart failure patients. As a result, the proposed method may also be able to diagnose AF patients satisfactorily, serving a significantly larger group of patients than conventional echocardiography. Finally, because the method uses a regular tissue Doppler ultrasound imaging scheme, it is considered as safe for the patient as conventional pulsed wave tissue Doppler imaging.

Because of the shear wave nature in which the particle velocity is directed perpendicular both to the wall and to the shear wave propagation direction, a parasternal view of the septal wall is preferred over an apical view. On the other hand, the imaging strategy can be optimized in an apical view to obtain both high spatial resolution and high temporal resolution in the narrower field of view compared with that needed for parasternal imaging (Brekke et al. 2014; Kanai 2005). Yet, the interpretation of such recording for shear wave tracking is not clear because the beam is almost perpendicular to the particle velocity. A systematic study of the effect of a parasternal versus an apical view on the tracking of the waves after mitral valve and aortic valve closure, combined with wave physics, should elucidate the underlying wave mechanics.

CONCLUSIONS

Using a high-frame-rate imaging sequence on a programmable commercial ultrasound machine, we recorded the mechanical waves after both mitral valve and aortic valve closure in the septal wall in the hearts of 22 healthy Göttingen minipigs. The waves had median propagation velocities of 2.2 m/s after mitral valve closure and 4.2 m/s after aortic valve closure. Such values are well in the range of those velocities measured invasively with shear wave imaging using acoustic radiation force, which shows the potential of the *non-invasive* method described in this article.

Acknowledgments—This research was supported by the Netherlands Organisation for Scientific Research (104002004) (NWO, Heartin4D by ZonMW). The position of I.H. and the animals were supported by the Academy of Finland (251272), Finnish Diabetes Research

Foundation, Finnish Foundation for Cardiovascular Research and European Commission FP7-Health-2010 Grant MEDIA-261409.

SUPPLEMENTARY DATA

Supplementary data related to this article can be found at http://dx.doi.org/10.1016/j.ultrasmedbio.2016.11.015.

REFERENCES

Arnott P, Pfeiffer G, Tavel M. Spectral analysis of heart sounds: relationships between some physical characteristics and frequency spectra of first and second heart sounds in normals and hypertensives. J Biomed Eng 1984;6:121–128.

Bercoff J, Tanter M, Fink M. Supersonic shear imaging: A new technique for soft tissue elasticity mapping. IEEE Trans Ultrason Ferroelectr Freq Control 2004a;51:396–409.

Bercoff J, Tanter M, Muller M, Fink M. The role of viscosity in the impulse diffraction field of elastic waves induced by the acoustic radiation force. IEEE Trans Ultrason Ferroelectr Freq Control 2004b;51:1523–1536.

Bercoff J, Montaldo G, Loupas T, Savery D, Meziere F, Fink M, Tanter M. Ultrafast compound Doppler imaging: Providing full blood flow characterization. IEEE Trans Ultrason Ferroelectr Freq Control 2011;58:134–147.

Bouchard RR, Hsu SJ, Wolf PD, Trahey GE. In vivo cardiac, acoustic-radiation-force-driven, shear wave velocimetry. Ultrason Imaging 2009;31:201–213.

Brekke B, Nilsen LC, Lund J, Torp H, Bjastad T, Amundsen BH, Stoylen A, Aase SA. Ultra-high frame rate tissue Doppler imaging. Ultrasound Med Biol 2014;40:222–231.

Couade M, Pernot M, Messas E, Bel A, Ba M, Hagège A, Fink M, Tanter M. In vivo quantitative mapping of myocardial stiffening and transmural anisotropy during the cardiac cycle. IEEE Trans Med Imaging 2011;30:295–305.

Hansen HHG, Saris AECM, Vaka NR, Nillesen MM, de Korte CL. Ultrafast vascular strain compounding using plane wave transmission. J Biomech 2014;47:815–823.

Holfort IK, Gran F, Jensen JA. Plane wave medical ultrasound imaging using adaptive beamforming. In: SAM 2008: 5th IEEE Sensor Array and Multichannel Signal Processing Workshop. New York: IEEE; 2008. p. 288–292.

Hollender PJ, Wolf PD, Goswami R, Trahey GE. Intracardiac echocardiography measurement of dynamic myocardial stiffness with shear wave velocimetry. Ultrasound Med Biol 2012;38:1271–1283.

Jiang Y, Guccione JM, Ratcliffe MB, Hsu EW. Transmural heterogeneity of diffusion anisotropy in the sheep myocardium characterized by MR diffusion tensor imaging. Am J Physiol Heart Circ Physiol 2007; 293:H2377–H2384.

Kanai H. Propagation of spontaneously actuated pulsive vibration in human heart wall and *in vivo* viscoelasticity estimation. IEEE Trans Ultrason Ferroelectr Freq Control 2005;52:1931–1942.

Kanai H. Propagation of vibration caused by electrical excitation in the normal human heart. Ultrasound Med Biol 2009;35:936–948.

Kjaergaard J, Korinek J, Belohlavek M, Oh JK, Sogaard P, Hassager C. Accuracy, reproducibility, and comparability of Doppler tissue imaging by two high-end ultrasound systems. J Am Soc Echocardiogr 2006;19:322–328.

Kruizinga P, Mastik F, de Jong N, van der Steen AF, van Soest G. Plane-wave ultrasound beamforming using a nonuniform fast Fourier transform. IEEE Trans Ultrason Ferroelectr Freq Control 2012;59:2684–2691.

Lu JY. 2D and 3D high frame rate imaging with limited diffraction beams. IEEE Trans Ultrason Ferroelectr Freq Control 1997;44: 839–856.

Mosterd A, Hoes A, De Bruyne M, Deckers J, Linker D, Hofman A, Grobbee D. Prevalence of heart failure and left ventricular dysfunction in the general population: The Rotterdam Study. Eur Heart J 1999;20:447–455.

National Research Council. NIH guide for the care and use of laboratory animals. Washington, DC: National Academic Press; 2011.

Nenadic IZ, Urban MW, Aristizabal S, Mitchell SA, Humphrey TC, Greenleaf JF. On Lamb and Rayleigh wave convergence in viscoelastic tissues. Phys Med Biol 2011;56:6723.

Nenadic I, Urban MW, Qiang B, Chen S, Greenleaf J. Model-free quantification of shear wave velocity and attenuation in tissues and its *in vivo* application. J Acoust Soc Am 2013;134:4011.

Papadacci C, Pernot M, Couade M, Fink M, Tanter M. High-contrast ultrafast imaging of the heart. IEEE Trans Ultrason Ferroelectr Freq Control 2014;61:288–301.

Parker K, Doyley M, Rubens D. Imaging the elastic properties of tissue: the 20 year perspective. Phys Med Biol 2011;56:R1.

Paulus WJ, Tschope C, Sanderson JE, Rusconi C, Flachskampf FA, Rademakers FE, Marino P, Smiseth OA, De Keulenaer G, Leite-Moreira AF, Borbely A, Edes I, Handoko ML, Heymans S, Pezzali N, Pieske B, Dickstein K, Fraser AG, Brutsaert DL. How to diagnose diastolic heart failure: A consensus statement on the diagnosis of heart failure with normal left ventricular ejection fraction by the Heart Failure and Echocardiography Associations of the European Society of Cardiology. Eur Heart J 2007;28:2539–2550.

Pernot M, Fujikura K, Fung-Kee-Fung SD, Konofagou EE. ECG-gated, mechanical and electromechanical wave imaging of cardiovascular tissues in vivo. Ultrasound Med Biol 2007;33:1075–1085.

Pislaru C, Pellikka PA, Pislaru SV. Wave propagation of myocardial stretch: Correlation with myocardial stiffness. Basic Res Cardiol 2014;109:1–12.

Pislaru C, Urban MW, Nenadic I, Greenleaf JF. Shearwave dispersion ultrasound vibrometry applied to *in vivo* myocardium. Conf Proc IEEE Eng Med Biol Soc 2009;2891–2894.

Provost J, Lee WN, Fujikura K, Konofagou EE. Imaging the electromechanical activity of the heart *in vivo*. Proc Natl Acad Sci USA 2011; 108:8565–8570.

Song P, Zhao H, Urban M, Manduca A, Pislaru SV, Kinnick RR, Pislaru C, Greenleaf J, Chen S. Improved shear wave motion detection using pulse-inversion harmonic imaging with a phased array transducer. IEEE Trans Med Imaging 2013;32:2299–2310.

Urban MW, Greenleaf JF. Use of the radon transform for estimation of shear wave speed. J Acoust Soc Am 2012;132:1982.

Urban MW, Pislaru C, Nenadic IZ, Kinnick RR, Greenleaf JF. Measurement of viscoelastic properties of *in vivo* swine myocardium using lamb wave dispersion ultrasound vibrometry (LDUV). IEEE Trans Med Imaging 2013;32:247–261.

van Dalen BM, Strachinaru M, van der Swaluw J, Geleijnse ML. A simple, fast and reproducible echocardiographic approach to grade left ventricular diastolic function. Int J Cardiovasc Imaging 2016;32:743–752.

Volker A. Plane wave imaging using phased array. In: 40th Annual Review of Progress in Quantitative Nondestructive Evaluation: Incorporating the 10th International Conference on Barkhausen Noise and Micromagnetic Testing. AIP Conf Proc 2014;1581:124–131.

Vos HJ, van Dalen BM, Bosch JG, van der Steen AFW, de Jong N. Myocardial passive shear wave detection. Proc IEEE Int Ultrason Symp 2015; http://dx.doi.org/10.1109/ULTSYM.2015.0152.